Spatially-Modulated Silicon Interface Energetics Via Hydrogen Plasma-Assisted Atomic Layer Deposition of Ultrathin Alumina

Alex Henning,* Johannes D. Bartl, Lukas Wolz, Maximilian Christis, Felix Rauh, Michele Bissolo, Theresa Grünleitner, Johanna Eichhorn, Patrick Zeller, Matteo Amati, Luca Gregoratti, Jonathan J. Finley, Bernhard Rieger, Martin Stutzmann, and Ian D. Sharp*

Atomic layer deposition (ALD) is a key technique for the continued scaling of semiconductor devices, which increasingly relies on scalable processes for interface manipulation of structured surfaces on the atomic level. While ALD allows the synthesis of conformal films with utmost control over the thickness, atomically-defined closed coatings and surface modifications are challenging to achieve because of 3D growth during nucleation. Here, a route is presented toward the sub-nanometer thin and continuous aluminum oxide (AlO$_x$) coatings on silicon substrates for the spatial control of the surface charge density and interface energetics. Trimethylaluminum in combination with remote hydrogen plasma is used instead of a gas-phase oxidant for the transformation of silicon dioxide (SiO$_2$) into alumina. Depending on the number of ALD cycles, the SiO$_2$ can be partially or fully transformed, which is exploited to deposit ultrathin AlO$_x$ layers in selected regions defined by lithographic patterning. The resulting patterned surfaces are characterized by lateral AlO$_x$/SiO$_2$ interfaces possessing 0.3 nm step heights and surface potential steps exceeding 0.4 V. In addition, the introduction of fixed negative charges of 9×10^{12} cm^{-2} enables modulation of the surface band bending, which is relevant to the field-effect passivation of silicon and low-impedance charge transfer across contact interfaces.

1. Introduction

Atomic layer deposition (ALD) has rapidly emerged as an essential tool in the semiconductor industry, since it provides highly conformal and precisely tunable coatings with sub-nanometer thickness control at low temperature. As such, ALD is a powerful method for integration of dielectrics in advanced optoelectronics and it has proved critical for the realization of emerging non-planar electronic devices.[1] In particular, amorphous aluminum oxide (AlO$_x$), which can be conformally grown by ALD on structured surfaces, is widely used in semiconductor technology for dielectric and chemical passivation,[2] carrier-selective charge transfer across the interfaces of silicon (Si) solar cells,[3] and gate dielectrics in non-planar field-effect transistors,[4] as well as for diffusion barriers and protective coatings.[5] When applied as a surface coating for field-effect passivation of Si, ALD AlO$_x$ introduces a

A. Henning, J. D. Bartl, L. Wolz, M. Christis, F. Rauh, M. Bissolo,
T. Grünleitner, J. Eichhorn, J. J. Finley, M. Stutzmann, I. D. Sharp
Walter Schottky Institute and Physics Department
Technical University of Munich
85748 Garching, Germany
E-mail: alex.henning@wsi.tum.de; sharp@wsi.tum.de

J. D. Bartl, B. Rieger
Department of Chemistry
WACKER-Chair for Macromolecular Chemistry
Technische Universität München
Lichtenbergstraße 4, 85747 Garching bei München, Germany

The ORCID identification number(s) for the author(s) of this article can be found under https://doi.org/10.1002/admi.202202166.

J. D. Bartl
Department of Chemistry and Bar-Ilan Institute for Nanotechnology &
Advanced Materials
Bar-Ilan University
Anna and Max Webb Street, Ramat Gan 5290002, Israel

P. Zeller, M. Amati, L. Gregoratti
Elettra-Sincrotrone Trieste SCpA
SS14-Km163.5 in Area Science Park, Trieste 34149, Italy

P. Zeller
Helmholtz-Zentrum Berlin für Materialien und Energie GmbH
BESSY II, Albert-Einstein-Straße 15, 12489 Berlin, Germany

P. Zeller
Fritz-Haber-Institut der Max-Planck-Gesellschaft
Dept. Inorganic Chemistry
Faradayweg 4–6, 14195 Berlin, Germany

high fixed negative charge density ($10^{12} - 10^{13}$ cm^{-2}),[6] which repels electrons from the surface and suppresses surface recombination via the field-effect, thereby improving the efficiency of Si solar cells.[2a,6,7] Recently, ultrathin AlO$_x$ has also been implemented as an interlayer for hole-selective tunnel contacts to p-doped Si, which has been shown to further improve the performance of Si solar cells.[3c,8]

Chemical bonding directly at the SiO$_2$/AlO$_x$ interface predominantly governs the negative charge and interface state density, whereas the bond coordination within the dielectric film remains unchanged away from the interface.[6,9] As a consequence, relatively thin ALD AlO$_x$ layers (several monolayers) can be used for field-effect passivation of p-doped Si, with such thin films exhibiting a similar impact as much thicker AlO$_x$ films.[2b,8c,10] However, sub-nanometer thin and conformal ALD coatings are challenging to achieve due to precursor steric effects and non-uniform distributions of available binding sites on the sample surface, which lead to 3D island growth during the nucleation regime.[2b] Therefore, significantly lower fixed negative charge is introduced at the Si/SiO$_2$/AlO$_x$ interface for few-cycle ALD processes[8c] since the deposited AlO$_x$ films tend to be discontinuous.[10b] Beyond field effect passivation, the challenge of creating sub-nanometer thin and continuous ALD layers limits the ability to engineer semiconductor interfaces at this length scale, which is of critical importance for future device downscaling and low-impedance tunnel contacts.

In this work, we demonstrate an alternative approach to engineer Si surface energetics via ALD of ultrathin and conformal AlO$_x$ coatings formed during cyclic exposure to remote hydrogen (H$_2$) plasma and trimethylaluminum (TMA). Importantly, by using H$_2$ plasma instead of a gas-phase oxidant during ALD, AlO$_x$ formation is governed by the solid-state chemical reduction of the underlying SiO$_2$, resulting in an interconversion of the terminal oxide from SiO$_2$ to AlO$_x$. Here, in situ spectroscopic ellipsometry (SE) and quadrupole mass spectrometry (QMS) were used to elucidate the dominant growth mechanisms in both the few cycle limit and after extended ALD cycles, while X-ray photoelectron spectroscopy (XPS), atomic force microscopy (AFM), and surface photovoltage (SPV) measurements were used to characterize the AlO$_x$-terminated Si substrates. With the insights gained from in situ techniques, we demonstrate control of the AlO$_x$ thickness on a sub-nanometer level, resulting in significant modulation of the surface band bending (SBB) through the introduction of fixed negative charge relevant to the field-effect passivation of Si. Moreover, the presented TMA/H$_2$ process can be performed at temperatures below 100 °C and, thus, is compatible with lithographic patterning. Taking advantage of this feature, we demonstrate smooth charge density patterns via spatially selective exposure of Si/SiO$_2$ surfaces to successive cycles of TMA/H$_2$ plasma. The resulting patterned surfaces are characterized by lateral AlO$_x$/SiO$_2$ interfaces possessing step heights as small as 0.3 nm, surface potential steps in excess of 0.4 V, and in-plane electric field strengths of ≈3×10^4 V cm^{-1}. The ability to realize smooth dielectric and charge density patterns by low-temperature (LT) ALD in combination with lithographic techniques, provides an intriguing possibility for creating carrier-selective contacts in Si solar cells and local gate structures in advanced transistors, as

well as for spatially-defined surface functionalization[11] of relevance for area-selective deposition[12] and chemical sensing.[13]
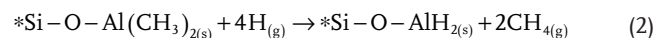
2. Results and Discussion

For the case of native oxide-terminated III-V semiconductors, the application of TMA or of TMA/H$_2$ plasma cycles prior to deposition of dielectric coatings has been demonstrated to reduce the density of interface states.[14] These so-called oxide clean-up processes rely on ligand exchange between the metalorganic precursor and the oxidic surface, which is promoted by the strong electropositivity of TMA. However, to the best of our knowledge, analogous processes have not been investigated for the case of oxide-terminated Si, despite its prominent importance in semiconductor technology.
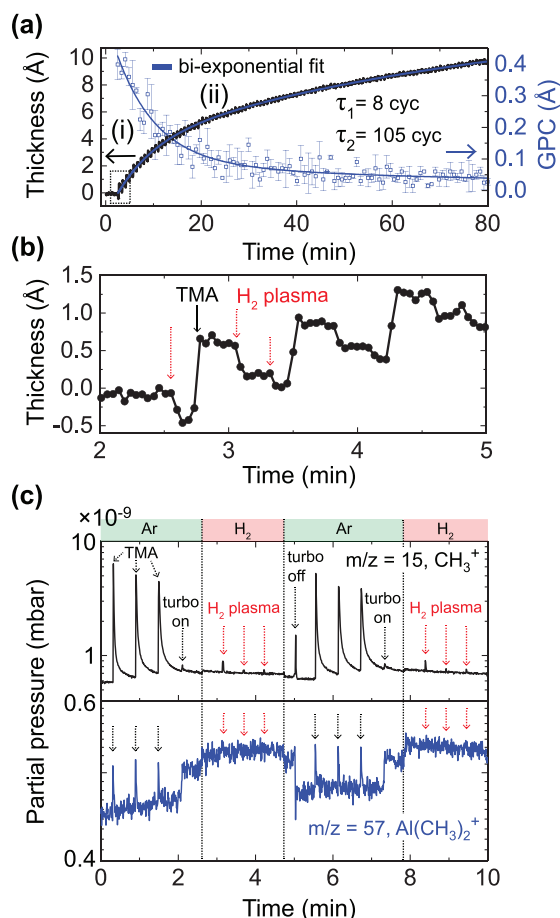
To gain mechanistic insights into the growth of AlO$_x$ on Si via successive exposure to TMA and remote H$_2$ plasma without the use of a gas-phase oxygen source, we tracked the ALD film thickness and reaction products in real-time by in situ SE and QMS, respectively, and assessed the surface chemical composition by XPS. The evolution of the AlO$_x$ growth, derived from SE (**Figure 1**a), reveals a steep decrease in the growth-per-cycle (GPC) during the initial ≈10 cycles (at 200 °C), followed by a relatively slow decay of the growth rate during subsequent cycles. The decay in the growth rate throughout the deposition is well approximated with a bi-exponential function, suggesting two concurrent processes with distinct reaction rates. As such, we distinguish two AlO$_x$ growth regimes (denoted as (i) and (ii) in Figure 1a), in which different surface chemical reactions dominate. The rapid decrease of the GPC during the initial cycles within regime (i) is consistent with a substrate-enhanced mechanism, and the consumption of the available binding sites (i.e., Si-O-H and Si-O groups) on the native SiO$_2$ terminated Si substrate,[15] while the formation of AlO$_x$ during growth regime (ii) is governed by diffusion-limited mass transport of oxygen from the underlying solid, as discussed in detail below.

Before film deposition, the Si substrate surface was cleaned in the growth chamber with a low-intensity remote H$_2$ plasma treatment (Figure 1b; Figure S1, Supporting Information), resulting in a more hydrophilic (hydroxylated) surface (Table S1, Supporting Information).[16] Subsequent exposure to TMA is known to lead to self-limiting adsorption of TMA according to the following reaction:[17]

$$*Si-OH_{(s)} + Al(CH_3)_{3(g)} \rightarrow *Si-O-Al(CH_3)_{2(s)} + CH_{4(g)} \qquad (1)$$
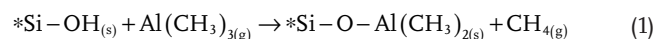
Reaction 1 is one of several possible chemical routes for the adsorption of TMA on a hydroxylated surface.[17a] For the case of traditional AlO$_x$ ALD processes, subsequent exposure of *Si-O-Al(CH$_3$)$_2$ to H$_2$O leads to the regeneration of a hydroxyl-terminated surface in the form of *Al-OH, onto which TMA can bind in a subsequent half cycle.[17a] However, in the present work, the surface is exposed to a remote H$_2$ plasma rather than a gas phase oxidant. Nevertheless, in situ QMS (Figure 1c) indicates the evolution of CH$_4$, consistent with the following proposed sequential reaction within growth regime (i):[18]

$$*Si-O-Al(CH_3)_{2(s)} + 4H_{(g)} \rightarrow *Si-O-AlH_{2(s)} + 2CH_{4(g)} \qquad (2)$$

**ADVANCED
SCIENCE NEWS**

www.advancedsciencenews.com

**ADVANCED
MATERIALS
INTERFACES**

www.advmatinterfaces.de

Figure 1. a) Evolution of the AlO$_x$ thickness (black line) and the GPC (blue squares), derived from in situ SE, are shown for 100 cycles of consecutive exposure to TMA and remote H$_2$ plasma (100 W) at 200 °C. The decay in the GPC is approximated with a bi-exponential function that shows two concurrent mechanistic processes, indicated by regions (i) and (ii). b) Zoom into the modeled thickness for three sequential cycles, indicating the impact of the TMA and H$_2$ exposure. c) Tracking of the by-products during the introduction of TMA (3×) and H$_2$ plasma (3×) into the reactor chamber by in situ mass spectrometry. The CH$_3^+$ ions with a mass-to-charge (m/z) ratio of 15 stem from Al(CH$_3$)$_3$ (i.e., TMA) or CH$_4$, while Al(CH$_3$)$_2^+$ ions at m/z of 57 originate from TMA.

Upon additional cycling, the deposition rate within regime (i) decreases as Si-OH surface sites are consumed since the Al-terminated sites are considerably less reactive with TMA.[14e] This proposed reaction pathway is supported by a comparative in situ SE experiment, in which the surface was exposed to an oxygen (O$_2$) plasma following 20 cycles of TMA/H$_2$ plasma (Figure S1, Supporting Information). Such a process results in an increase of the film thickness due to oxidation of Al-terminated surface sites. We note that this behavior is consistent with our prior work on GaN surfaces, in which a similar lack of TMA chemisorption after TMA/H$_2$ plasma exposure resulted in self-saturating deposition of an AlO$_x$ monolayer.[14e]

Importantly, we find that the reactive hydrogen radicals generated by the H$_2$ plasma are essential for the release of the alkyl ligands of TMA via the generation of CH$_4$. To verify this, we performed a reference deposition using argon (Ar) plasma instead of H$_2$ plasma (Figure S1 and S2, Supporting Information).

Despite the lack of reactive gas species, in situ SE reveals an increase of film thickness with cycle number (Figure S1, Supporting Information). Although the apparent alumina growth rate is larger for the Ar plasma process than for H$_2$ plasma process, subsequent O$_2$ plasma exposure (Figure S1, Supporting Information) leads to a significant reduction of the film thickness for the TMA/Ar plasma process. Moreover, in situ QMS reveals a threefold reduction in the amount of methane (CH$_4$) released during the plasma step of the TMA/Ar process in comparison to the TMA/H$_2$ process (Figure S2, Supporting Information). These findings suggest that the TMA/Ar plasma process results in significant carbon incorporation due to physical decomposition of adsorbed TMA, with subsequent O$_2$ plasma exposure leading to volatilization of carbon impurities. In contrast, no such decrease in film thickness upon O$_2$ plasma exposure was observed for the AlO$_x$ film grown by the TMA/H$_2$ process (Figure S1, Supporting Information), indicating formation of AlO$_x$ with minimal carbon impurities, as confirmed by XPS (Figure S3a, Supporting Information). Thus, we conclude that Reaction 2 is a critical step for ligand removal during ALD alumina growth in the absence of a gas-phase oxidant.

XPS provides additional insight into the nature of deposited AlO$_x$ films, as well as their mechanism of formation. Prior to ALD, the surface of the Si substrate is terminated by a native SiO$_2$ layer (**Figure 2**a). In addition to the dominant silicon oxide component at a binding energy (BE) of ≈103.3 eV, which is characteristic of SiO$_2$ (Si^{4+}), additional spectral contributions at lower BEs indicate the presence of sub-stoichiometric SiO$_x$, which has previously been associated with the Si/SiO$_2$ interface.[19] The XPS derived thickness of the SiO$_2$ layer (≈1.7 nm) agrees with the result obtained by SE (Table S1, Supporting Information), and was calculated with the model proposed by Hill et al.[20] using the integrated intensities of the silicon oxide components, I_{ox}, and silicon component, I_0, of the Si 2p core level spectrum (Figure 2a; Figure S3, Supporting Information). Following 20 cycles of TMA and remote H$_2$ plasma, the intensity ratio, I_{ox}/I_0, decreased (Figure 2b), indicating a partial reduction of the surface SiO$_2$, which is consistent with the thermodynamically favored solid-state redox reaction of TMA with SiO$_2$ ($\Delta G = -235$ kcal mol^{-1} at 300 °C).[21] Indeed, the calculated SiO$_2$ layer thickness decreased by ≈0.9 nm after the TMA/HP process. In contrast, application of conventional ALD of AlO$_x$ with TMA and H$_2$O at 200 °C reveals an increase of the SiO$_2$ thickness of ≈0.1 nm (Figure 2c; Table S1, Supporting Information). This result confirms the fundamentally different mechanism of AlO$_x$ growth using H$_2$ plasma compared to a gas phase oxidant (H$_2$O). In the former case, oxygen is supplied from the underlying SiO$_2$, resulting in its partial reduction.

In addition to the changing ratios of oxidized and elemental Si, the overall photoemission intensity from the Si 2p spectral region decreased following 20 TMA/H$_2$ plasma cycles due to attenuation by the overlayer (Figure S4, Supporting Information). Concomitantly, an additional O 1s component appeared (Figure S3b, Supporting Information) together with an Al 2p component at the characteristic BE of ≈75.5 eV for Al-O[22] (Figure 2b, inset). The resulting spectra are similar to those obtained from the conventional thermal TMA/H$_2$O process, thus confirming the formation of alumina on Si after the
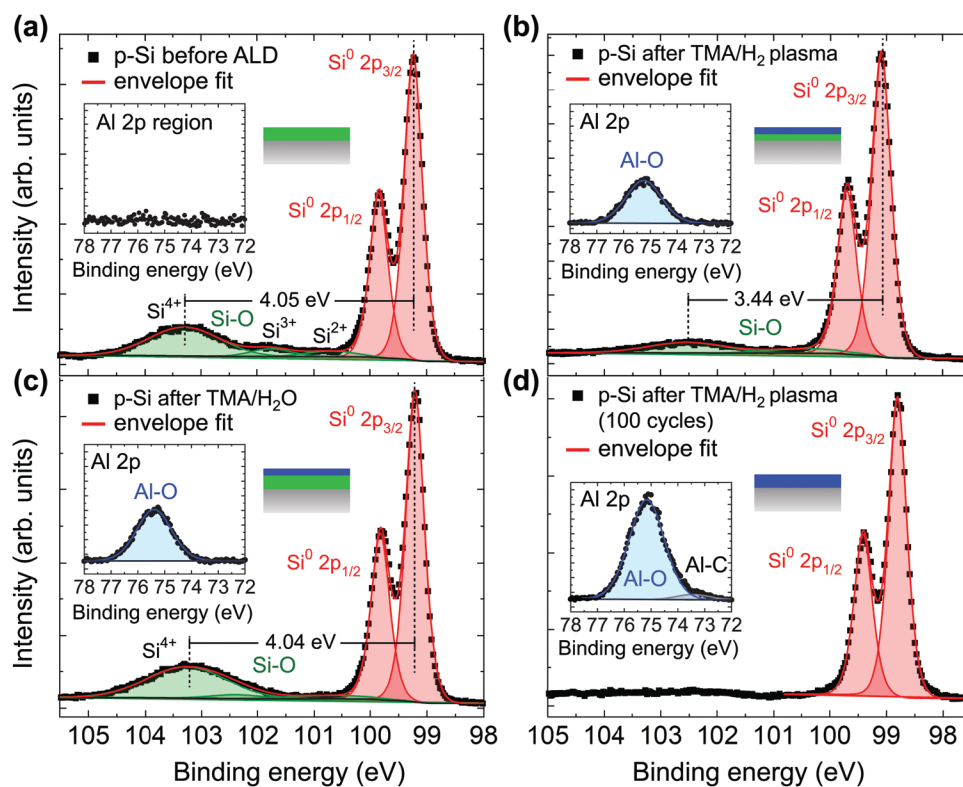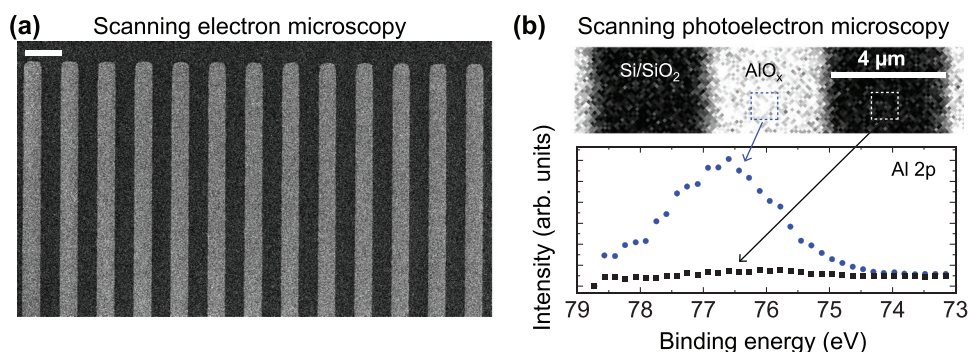
Figure 2. X-ray photoelectron spectra reveal the formation of aluminum oxide on a Si substrate following the transformation of the native SiO_2 layer after the TMA/H_2 plasma process. Si 2p core level spectrum of a Si substrate a) with native SiO_2 before ALD, b) after 20 cycles of TMA and remote H_2 plasma, c) following ALD with TMA and water, and (d) after 100 cycles of TMA and remote H_2 plasma. The ratio between elemental Si (Si^0) and SiO_2 (Si^{4+}) decreased after the TMA/H_2 plasma process, while it slightly increased after the TMA/H_2O process. The insets show the Al 2p core level region with the same intensity scale (y-axis) for comparison. The schematic cross-sections in the insets illustrate the Si substrate (grey) coated with silicon oxide (green), alumina (blue), or both oxide layers.

TMA/H_2 plasma process. Here, we note that the sample was transferred from the ALD system to the XPS chamber through ambient air, which resulted in the oxidation of initially generated $*Si-O-AlH_2$ or $*Si-O-Al(CH_3)H$ sites. Notably, the presence of AlO_x alters the surface chemistry of Si, resulting in a more hydrophilic surface, as indicated by the decrease in the static water contact angle from 64° for the bare Si substrate to 25° for the TMA/H_2 plasma-treated Si (Table S1, Supporting Information). In this way, the oxide conversion process can be exploited for subsequent (area-selective) chemical functionalization of the AlO_x-terminated surface, as recently reported by our group.[14e,23]

We next turn our attention to growth regime (ii) (Figure 1a), during which film deposition proceeded at a slow but nearly constant rate (≈0.05 Å/cycle), despite the absence of a gas-phase oxygen source. Importantly, X-ray photoelectron spectra from samples exposed to 100 cycles of the TMA/H_2 plasma process, which is well within regime (ii), indicate that the native SiO_2 layer on Si was fully reduced to elemental Si, leaving a Si substrate coated with AlO_x (Figure 2d). We note that other constituents, such as $AlSi_xO_y$ may be present,[9] but were not detectable with the XPS system used in this study. Such complete transformation of the ≈17 Å thick SiO_2 layer (Figure 1a), composed of several monolayers, implies the solid-state transport of atomic or molecular oxygen through the SiO_2 and AlO_x layers to the surface during the AlO_x growth process. This is con-

firmed by XPS analysis of a quartz substrate after TMA and H_2 plasma treatment, which reveals the presence of Si^0 (Figure S5, Supporting Information) and thus confirms the complete reduction of SiO_2 to elemental Si. The activation energy for the diffusion of molecular oxygen through SiO_2 has been predicted by density functional theory to be 0.3 eV,[24] which is lower than the reported activation energy of aluminum diffusion in amorphous SiO_2 of 0.73 eV.[25] Although the thermal energy at the growth temperature of 200 °C ($k_BT = 0.041$ eV) is significantly below the diffusion activation energies of both elements, it is far more likely for oxygen than for Al to diffuse within SiO_2.

In addition to the above considerations, a small shoulder indicative of aluminum carbide (AlC_x)[26] appears at low binding energies of the Al 2p core level region following 100 cycles of TMA/H_2 plasma (Figure 2d, inset). Based on these observations, we infer that oxygen extraction is facilitated by a strongly oxidizing surface layer (adsorbed TMA), and that complete depletion of the solid-state oxygen source after extended cycling leads to increased carbon contamination in the form of AlC_x due to the absence of an external oxidant. Thus, from the combined insights gained by QMS, SE, and XPS, we conclude that hydrogen plasma and TMA chemically react with the oxidized Si surface until there is a saturation of bindings sites (regime (i)) and subsequently until complete depletion of the oxygen (regime (ii)) from the native silicon oxide layer, thereby transforming the SiO_2 into Si capped with AlO_x.

ADVANCED
SCIENCE NEWS
www.advancedsciencenews.com

ADVANCED
MATERIALS
INTERFACES
www.advmatinterfaces.de

(a) Scanning electron microscopy

(b) Scanning photoelectron microscopy

Figure 3. a) Secondary electron SEM image of an AlO$_x$ pattern on Si substrate following 20 cycles of TMA and H$_2$ plasma at 70 °C. The bright regions correspond to AlO$_x$-terminated surfaces. The scale bar corresponds to 8 µm length. An electron acceleration voltage of 2.0 kV was used. b) Synchrotron-based SPEM map of the Al 2p core level. Each pixel (150 × 150 nm^2) represents a spectrum in the Al 2p core level spectral range of BEs from 79 – 73 eV. The sample was excited with photons of 638 eV energy. The photoelectron core level spectra (bottom) were retrieved from the marked square regions in the SPEM image. We note that the spectrum is shifted towards higher BE due to differential charging of the insulating AlO$_x$ layer.

While the surface oxide is reduced for the TMA/H$_2$ plasma process, it is oxidized for standard ALD AlO$_x$ processes using water (H$_2$O) or oxygen plasma,[10b,27] the latter of which generates defects and introduces detrimental interface states in Si.[28] Moreover, for LT ALD processes involving water as the oxidant source, condensation hampers self-limiting deposition and can reduce the film quality. Owing to the high vapor pressure and reactivity of TMA, as well as the self-limiting nature of the reactions of TMA and hydrogen radicals with the sample surface (Reaction 1 and 2), the ALD process can be performed at temperatures below 100 °C and is thus compatible with lithographic processing. Here, we exploited this feature to create dielectric micropatterns comprising distinct regions terminated with SiO$_2$ and AlO$_x$.

Scanning electron microscopy (SEM) and scanning photoelectron microscopy (SPEM) depict the AlO$_x$ pattern on a Si substrate (**Figure 3**). The SEM image (Figure 3a) shows a strong contrast between the two materials, AlO$_x$ and SiO$_2$, and confirms lithographic pattern fidelity after the lift-off process. Such a strong contrast in the SEM image, despite a sub-nanometer step height, can be explained with Dionne's model that predicts a larger secondary electron yield for ALD alumina than for SiO$_2$ (and Si) because of the higher material density, as well as the lower conductivity and electron affinity, of the former.[29] From the elemental map of the Al 2p region obtained by SPEM (Figure 3b), it is evident that alumina is deposited in spatially selected regions as no alumina signal (Al 2p) was detected within the Si/SiO$_2$ region.

To assess the uniformity and thickness of the AlO$_x$ coating on a nanometer-scale, we characterized the surface morphology and potential landscape of the AlO$_x$ patterns by AFM and Kelvin probe force microscopy (KPFM), respectively (**Figure 4**). Both the topography and the simultaneously acquired contact potential difference (CPD) maps are uniform within each region, demonstrating a continuous AlO$_x$ coating. The profile extracted from the AFM topograph (Figure 4c, top) shows a height difference between the uncoated and AlO$_x$-covered Si region of only 2.9 ± 0.3 Å, which is thinner than previously demonstrated for conformal ALD AlO$_x$ coatings on Si. Notably, both surfaces are smooth, exhibiting a root mean square (rms) roughness (R$_{rms}$) of 0.18 nm (Figure 4a,c). The fact that the surface remains
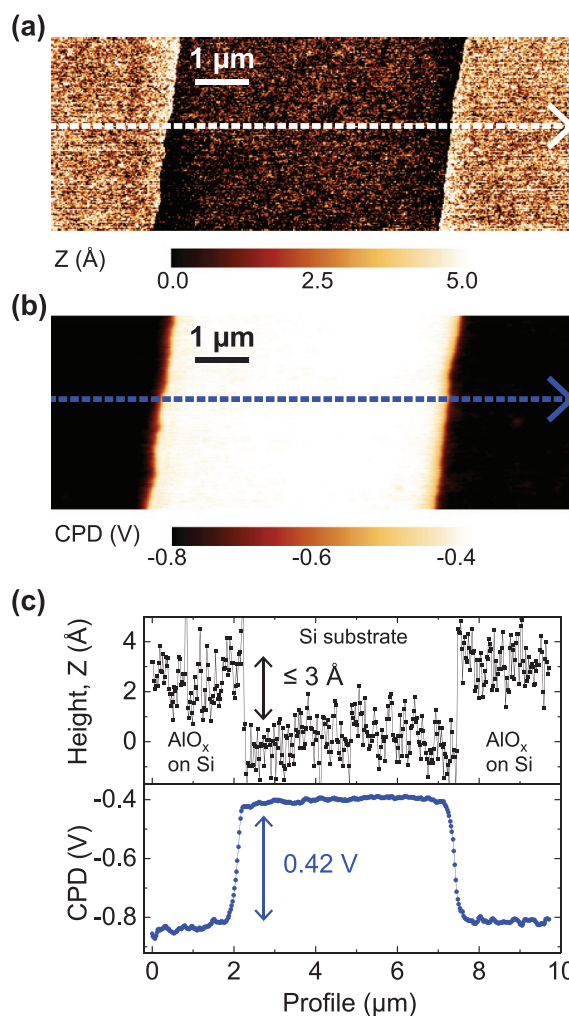
Figure 4. a) Intermittent contact mode AFM topography and b) frequency modulation KPFM image of the AlO$_x$ pattern on p-doped Si substrate. c) Topography and CPD profiles were taken along the lines, as indicated in the images of (a) and (b). While a step height of less than 3 Å exists across the lateral interface between AlO$_x$ and SiO$_2$ terminal surfaces, a surface potential step of 0.42 V arises due to fixed charge introduced by the TMA/H$_2$ ALD process (10 cycles).
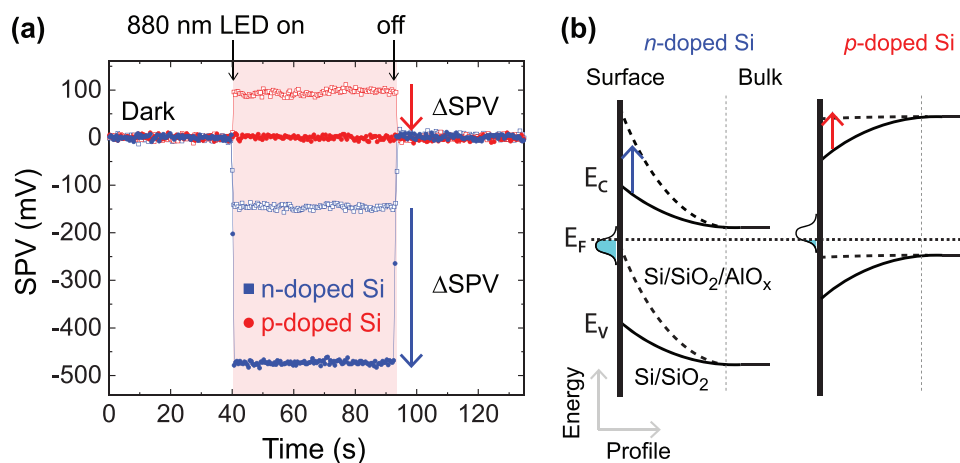
Figure 5. a) Plots of the SPV as a function of time upon switching the 880 nm illumination source on and off for *p*-doped Si (red) and *n*-doped Si (blue) before (open circles) and after (filled circles) processing by 20 cycles of TMA and remote H_2 plasma. The vertical arrows indicated the magnitude of SPV change induced by the 20 cycle TMA/H_2 plasma treatment for both *n*- and *p*-type Si. The SPV is determined by subtracting the CPD values measured under illumination and in the dark, SPV = CPD_{light} - CPD_{dark}. (b) Schematic energy band diagrams of *n*-doped Si (left) and *p*-doped Si (red).

smooth after the TMA/H_2 plasma process is an essential criterion for its implementation in Si semiconductor technology.

Importantly, application of the TMA/H_2 plasma process for the formation of a sub-nanometer thin AlO_x coating on Si substantially reduces its work function, as determined by KPFM. As such, this process provides opportunities to tune the energy band alignment at the Si interfaces, as discussed below. In particular, a similar decrease in the CPD of 0.4 V was measured for both *p*- and *n*-doped Si substrates following deposition of the AlO_x layer of different thicknesses (Figure 4; Figure S6, Supporting Information) and can be explained by the formation of a microscopic surface dipole, whose negative charges at the SiO_2/AlO_x interface[6] are compensated by the positive charges from the AlO_x-terminated surface in ambient. Thus, a microscopic dipole layer with its positive pole pointing outward leads to a decrease in the effective electron affinity, and the observed reduction of the CPD and work function of the AlO_x coated Si. Moreover, the potential profile across the patterned region reveals an abrupt potential step of ≈0.42 V, yielding an electric field of ≈3 × 10⁴ V cm⁻¹ at the lateral interface between bare and AlO_x-coated *p*-doped Si (Figure 4c, bottom), whose magnitude is determined by the photolithography process and is experimentally underestimated due to the finite tip radius of the platinum-iridium-coated Si tip of about ≈30 nm. Notably, the CPD is maintained over several months in ambient air as the same potential step has been repeatedly measured throughout this time.

The observed reduction of the work function after alumina deposition on Si and the introduction of negative fixed charges is consistent with prior investigations of conventional ALD using TMA and H_2O, which has shown that AlO_x deposited on Si introduces negative fixed charge that is beneficial for the field-effect passivation of *p*-doped Si.[2a] Therefore, we investigated how the ultrathin AlO_x coatings, synthesized via the TMA/H_2 process, affect the SBB of moderately doped Si substrates of relevance for Si photovoltaics. SPV measurements were conducted using a Kelvin probe that was coupled to a light source for above band gap illumination using an 880 nm

light emitting diode. As shown in **Figure 5**a, these measurements reveal a significant increase (decrease) of the SBB of a moderately *n*-doped (*p*-doped) Si substrate after 20 cycles of the TMA/H_2 process. These observations confirm the presence of considerable negative charge density introduced by the AlO_x. For the case of *p*-type material, holes are attracted to the surface by the fixed negative oxide charge, resulting in an accumulation layer and the complete elimination of a SPV (Figure 5b). Thus, ultrathin AlO_x formed by the TMA/H_2 process can be used for field-effect passivation of *p*-doped Si. In contrast, the fixed negative oxide charge repels electrons within *n*-type material, resulting in a significantly larger SBB (Figure 5b), which increased by 340 meV. Applying Poisson's equation and Gauss' theorem for the 1D model of *n*-type Si shown in Figure 5b with the measured SBB (Figure S5, Supporting Information), yields an increase in the fixed negative charge density at the AlO_x/SiO_2 interface of $Q_{it} = 9 \times 10^{12}$ cm⁻². We note that a similar increase of the SPV and SBB (350 mV) is achieved for *n*-type Si coated with a 1 nm thick AlO_x layer deposited with the TMA/H_2O process (Figure S7, Supporting Information). This finding suggests that remote H_2 plasma exposure (and reduction of the SiO_2 layer) during the TMA/H_2 process does not introduce additional electronic defects and that the negative fixed charges are indeed introduced at the SiO_2/AlO_x interface, in agreement with prior work.[2b,6,8c,9] Nanometer-thin alumina films, deposited by TMA and water, provide similar field effect passivation as the ones created with the TMA/H_2 process. However, the comparably thicker layers obtained with the TMA/H_2O process impede interfacial charge carrier transport[30] and would lead to larger lateral step heights when patterned.

3. Conclusion

In summary, we presented an ALD process based on TMA and remote hydrogen plasma to convert the native oxide on Si into alumina. This gas-phase process is scalable and omits wet-chemical treatments, thus providing a simple path to interface

**ADVANCED
SCIENCE NEWS**

www.advancedsciencenews.com

**ADVANCED
MATERIALS
INTERFACES**

www.advmatinterfaces.de

engineering in Si electronics. In particular, the sub-nanometer thin continuous AlO_x coatings on silicon were demonstrated for field-effect passivation, and can be potentially utilized for carrier-selective transport across contact interfaces. Furthermore, the selective deposition in lithographically defined areas at low temperatures allowed us to locally modify the dielectric environment and surface chemistry of Si substrates. The presented gas-phase processing concept provides new opportunities for engineered interfaces of relevance for surface functionalization of (bio)chemical sensors, control of charge carrier transport and field-effect passivation at Si interfaces, and defining gate structures for local control of charge carriers via field-effect. In addition, the ultrathin AlO_x coating can be potentially used as a buffer layer to relax lattice matching constraints in the synthesis of semiconductor heterostructures, as previously shown for gallium nitride.[31]

4. Experimental Section

Silicon Substrates: Moderately *n*-doped (As) and *p*-doped (B) Si substrates (Siegert Wafer, Germany) with a <100> crystal orientation and a resistivity of $\approx$6 Ω cm were used for this study. The frontside surfaces were chemo-mechanically polished by the manufacturer, and were terminated with a 1–2 nm thick native oxide layer. The thicknesses of the oxide layers were determined by SE and XPS.

Ohmic contacts were applied to the backsides of the Si wafers by metal evaporation and annealing. Immediately prior to mounting samples in the evaporator, Si backside surfaces were etched in 5% HF solution to remove the oxide and provide passive H-terminated surfaces. All metallization procedures were carried out using thermal evaporation at rates between 1 and 3 Å/s under vacuum (<10^{-6} mbar). For *n*-type Si, 100 nm of Al was evaporated onto the backside of the wafer before annealing in vacuum ($\approx 10^{-6}$ mbar) at 500 °C for 5 min in a rapid thermal annealer. For *p*-type Si, 100 nm of a $Au_{0.99}Sb_{0.01}$ alloy was evaporated and annealed under the same conditions, resulted the formation of a AuSi eutectic. Following Ohmic contact formation, 10 nm Ti and 100 nm Au were evaporated onto the backside surface to provide a homogeneous and conductive interface. Highly *n*-doped (As) and *p*-doped (B) Si substrates (Siegert Wafer, Germany) with a <100> crystal orientation and a resistivity of $\approx$0.005 Ω cm were used for KPFM.

Optical Lithography: Lithographic lift-off processing was combined with LT plasma-assisted ALD to define a micropattern of AlO_x on the frontside of Si substrates. A resist double layer consisting of polydimethyl glutarimide (PMGI SF3, Microchem) and ma-P 1205 (micro resist technology) was patterned with a maskless aligner (Heidelberg, MLA100) and developed in tetramethylammonium hydroxide (TMAH, micro resist technology). Lift-off was performed by ultrasonication (10 min, 40 °C) in n-methyl-2-pyrrolidone (micro resist technology).

Atomic Layer Deposition: Plasma-assisted ALD was carried out in a hot-wall reactor (Fiji G2, Veeco) at either 200 or 70 °C using Ar (99.9999%, Linde) as the carrier and purge gas. AlO_x was formed on the Si substrate following sequential exposure to TMA (99.999%, Strem) and remote hydrogen plasma that was generated with a sapphire-based inductively coupled plasma source. The TMA half-cycle was carried out at a background pressure of 0.09 Torr and at a peak pressure of 0.16 Torr, after which the second half-cycle comprised two consecutive H_2 plasma exposures at 100 W at a background pressure of 0.01 Torr for a duration of 2 s (3s). In a separate process, TMA and deionized water (HPLC grade, Sigma Aldrich) were used for conventional thermal ALD of alumina at 200 °C. For all processes, purging between half cycles was performed using flowing Ar (110 sscm, 0.09 Torr) for 15 s. The purge time was set to 15 or 60 s for ALD processes carried out at a reactor temperature of 200 or 70 °C, respectively. For all substrates, in situ cleaning of Si surfaces

via remote hydrogen plasma exposure (100 W, 20 sscm, 0.3 Torr) was performed to remove adventitious organic contamination and activate the surface.[16]

Spectroscopic Ellipsometry: Changes in the adlayer and film thickness on the Si substrates were monitored in situ during ALD with a sampling time of $\approx$3 s using a spectroscopic ellipsometer (M-2000, J. A. Woollam). The light of a Xenon lamp (Hamamatsu, L2174-01) was focused to a spot area of $\approx 5\times 8$ mm^2 onto the substrate surface. The incoming and reflected light passed through fused silica windows (Lesker, VPZL-275DU) arranged in a fixed angle (67°) geometry. The thickness of the SiO_2 layers and the ALD AlO_x film were obtained by analyzing the ellipsometry spectra with established optical models for Si and SiO_2, and by using a Cauchy model for the AlO_x layer. The mean GPC values and standard deviations were determined as follows. In the first step, an ALD thickness was obtained for every measurement point of the time series by modeling the in situ SE data with known optical parameters (Supporting Information). In the second step, GPC values were calculated by subtracting the thickness values, obtained during the argon purge step, between two consecutive cycles. Finally, four GPC values were averaged. In situ SE was repeated on three Si/SiO$_2$ substrates for the TMA/H$_2$ process and each experiment showed the same quantitative behavior. Additional experimental details are provided in the Supporting Information.

X-ray Photoelectron Spectroscopy: XPS spectra were acquired in the hybrid lens mode at a pass energy (PE) of 10 eV, and a take-off angle of 0° with a Kratos Axis Supra setup equipped with a monochromatic Al Kα X-ray source (photon energy = 1486.7 eV) operated with an emission current of 15 mA. The beam area was set to $\approx 2 \times 1$ mm^2 using the slot collimation mode. The BE was calibrated with in situ sputter-cleaned Ag, Au, and Cu standard samples. Thereby, the kinetic energies of the Ag 3d (1118.51 eV), Au 4f (1402.73 eV), and Cu 2p (554.07 eV) core levels were referenced with an accuracy of 25 meV to the known peak values. Charge neutralization was not required, as no BE shifts indicative of (differential) charging were observed for the doped Si substrates. Each sample was measured at three different locations, and the extracted SiO_2 thicknesses were averaged to obtain a mean thickness and standard deviation for each sample (Table S1, Supporting Information).

Quadrupole Mass Spectrometry: To detect gas phase species in situ during ALD, mass spectrometry experiments were conducted with a Hiden mass spectrometer (HPR-30), equipped with two detectors, a Faraday cup, and a secondary electron multiplier, the latter of which was used for all experiments. The tube (diameter 5 cm) connecting the mass spectrometer to the reactor was heated to above 120 °C. An orifice with an opening of 0.05 mm was used.

Surface Photovoltage Measurements: SPV measurements were carried out in ambient air at room temperature using a commercial setup (KP, KP Technology) in a closed faraday cage. The Si substrate was illuminated with a focused light-emitting diode with a wavelength of 880 nm (M340L4, Thorlabs) and an intensity of $\approx$35 mWcm^{-2}. A piezoelectrically driven gold probe with a tip diameter of 50 μm and a work function of $\approx$4.9 eV was used as the measurement electrode. The time resolution of the CPD measurements was 1.0 s.

Scanning Photoelectron Microscopy: Synchrotron-based SPEM measurements were performed at the ESCA microscopy beamline at the Elettra synchrotron (Trieste, Italy). Technical details of the SPEM setup were described in a previous report.[32] In brief, the X-ray photon energy was set to 638 eV with a (Gaussian) X-ray focal radius of $\approx$150 nm and PE of 20 eV, resulting in an instrumental broadening of 0.35 eV determined by the Au 4f core level emission from an internal gold standard. Maps were acquired by using a multichannel delay line detector, allowing the acquisition of a spectrum in snap-shot mode at every pixel of the map. Photoelectron spectra were extracted from the SPEM images by averaging over an area of $\approx$0.9 μm^2 (i.e., 6 × 6 pixels or 36 point spectra) using the software Igor Pro (v. 8.0.4.2).

Scanning Electron Microscopy: The SEM images were acquired with an NVision 40 FIB-SEM from Carl Zeiss using the in-lens secondary electron detector and an electron beam acceleration voltage of 2.0 kV.

Atomic Force Microscopy and Kelvin Probe Force Microscopy: AFM and KPFM measurements were carried out with a Bruker Multimode V microscope (Billerica, MA, USA) in ambient using platinum/iridium (95/5) coated AFM probes (PPP EFM, Nanosensors) with a nominal tip radius of 20 nm, typical resonance frequency of 75 kHz and force constant of 2.8 N m^{-1}. Height images (12×12 μm^2) were acquired at a scan rate of 0.3 Hz with 512 point sampling. High-resolution images were obtained with a 2×2 μm^2 scan with 512 point sampling using an uncoated Si tip with ≈10 nm tip radius. The height and CPD profiles were obtained by averaging over 10 scan lines (each line probed with 512 sampling points) using the software Gwyddion (v. 2.55). The average step heights were determined from AFM measurements of two patterned Si substrates that were manufactured following the same process.

Conflict of Interest

The authors declare no conflict of interest.

Author Contributions

All authors have given approval to the final version of the manuscript.

Data Availability Statement

The data that support the findings of this study are available from the corresponding author upon reasonable request.

[1] R. A. Ovanesyan, E. A. Filatova, S. D. Elliott, D. M. Hausmann, D. C. Smith, S. Agarwal, *J. Vac. Sci. Technol., A* **2019**, *37*, 060904.

[2] a) J. Schmidt, A. Merkle, R. Brendel, B. Hoex, M. C. M. van de Sanden, W. M. M. Kessels, *Prog. Photovoltaics* **2008**, *16*, 461; b) V. Naumann, M. Otto, R. B. Wehrspohn, C. Hagendorf, *J. Vac. Sci. Technol. A* **2012**, *30*, 04D106.

[3] a) Z. Xin, Z. P. Ling, N. Nandakumar, G. Kaur, C. Ke, B. Liao, A. G. Aberle, R. Stangl, *Jpn. J. Appl. Phys.* **2017**, *56*, 08MB14; b) K. Liu, O. Cristini-Robbe, O. I. Elmi, S. L. Wang, B. Wei, I. Yu, X. Portier, F. Gourbilleau, D. Stiévenard, T. Xu, *Nanoscale Res. Lett.* **2019**, *14*, 8; c) Z. Xin, Z. P. Ling, P. Wang, J. Ge, C. Ke, K. B. Choi, A. G. Aberle, R. Stangl, *Sol. Energy Mater. Sol. Cells* **2019**, *191*, 164.

[4] J. Feng, G. Thareja, M. Kobayashi, S. Chen, A. Poon, Y. Bai, P. B. Griffin, S. S. Wong, Y. Nishi, J. D. Plummer, *IEEE Electron Device Lett.* **2008**, *29*, 805.

[5] a) R. Fan, W. Dong, L. Fang, F. Zheng, X. Su, S. Zou, J. Huang, X. Wang, M. Shen, *Appl. Phys. Lett.* **2015**, *106*, 013902; b) L. Helmich, D. C. Walter, D. Bredemeier, J. Schmidt, *Phys. Status Solidi RRL* **2020**, *14*, 2000367.

[6] D. K. Simon, P. M. Jordan, T. Mikolajick, I. Dirnstorfer, *ACS Appl. Mater. Interfaces* **2015**, *7*, 28215.

[7] D. Damianos, G. Vitrant, A. Kaminski-Cachopo, D. Blanc-Pelissier, G. Ghibaudo, M. Lei, J. Changala, A. Bouchard, X. Mescot, M. Gri, S. Cristoloveanu, I. Ionica, *J. Appl. Phys.* **2018**, *124*, 125309.

[8] a) B. E. Davis, N. C. Strandwitz, *IEEE J. Photovolt* **2020**, *10*, 722; b) K. Öğütman, N. Iqbal, G. Gregory, M. Li, M. Haslinger, E. Cornagliotti, W. V. Schoenfeld, J. John, K. O. Davis, *Phys. Status Solidi A* **2020**, *217*, 2000348; c) D. Hiller, J. Göttlicher, R. Steininger, T. Huthwelker, J. Julin, F. Munnik, M. Wahl, W. Bock, B. Schoenaers, A. Stesmans, D. König, *ACS Appl. Mater. Interfaces* **2018**, *10*, 30495.

[9] K. Kim, N. Nandakumar, X. Zheng, S. Lim, Z. Hameiri, *IEEE J. Photovolt* **2021**, *11*, 620.

[10] a) N. M. Terlinden, G. Dingemans, M. C. M. van den Sanden, W. M. M. Kessels, *Appl. Phys. Lett.* **2010**, *96*, 112101; b) F. Werner, B. Veith, D. Zielke, L. Kühnemund, C. Tegenkamp, M. Seibt, R. Brendel, J. Schmidt, *J. Appl. Phys.* **2011**, *109*, 113701.

[11] A. Vilan, D. Cahen, *Chem. Rev.* **2017**, *117*, 4624.

[12] T.-L. Liu, S. F. Bent, *Chem. Mater.* **2021**, *33*, 513.

[13] a) D. Blaschke, S. Pahlow, T. Fremberg, K. Weber, A. D. Müller, S. Kurz, J. Spohn, V. Dhandapani, L. Rebohle, I. Skorupa, H. Schmidt, *Appl. Surf. Sci.* **2021**, *545*, 148729; b) J. D. Bartl, P. Scarbolo, D. Brandalise, M. Stutzmann, M. Tornow, L. Selmi, A. Cattani-Scholz, *Langmuir* **2019**, *35*, 3272.

[14] a) S. Klejna, S. D. Elliott, *J. Phys. Chem. C* **2012**, *116*, 643; b) A. D. Carter, W. J. Mitchell, B. J. Thibeault, J. J. M. Law, M. J. W. Rodwell, *Appl. Phys. Express* **2011**, *4*, 091102; c) L. B. Ruppalt, E. R. Cleveland, J. G. Champlain, S. M. Prokes, J. B. Boos, D. Park, B. R. Bennett, *Appl. Phys. Lett.* **2012**, *101*, 231601; d) S. Gu, E. A. Chagarov, J. Min, S. Madisetti, S. Novak, S. Oktyabrsky, A. J. Kerr, T. Kaufman-Osborn, A. C. Kummel, P. M. Asbeck, *Appl. Surf. Sci.* **2014**, *317*, 1022; e) A. Henning, J. D. Bartl, A. Zeidler, S. Qian, O. Bienek, C.-M. Jiang, C. Paulus, B. Rieger, M. Stutzmann, I. D. Sharp, *Adv. Funct. Mater.* **2021**, *31*, 2101441.

[15] R. L. Puurunen, W. Vandervorst, *J. Appl. Phys.* **2004**, *96*, 7686.

[16] V. Gupta, N. Madaan, D. S. Jensen, S. C. Kunzler, M. R. Linford, *Langmuir* **2013**, *29*, 3604.

[17] a) R. L. Puurunen, *J. Appl. Phys.* **2005**, *97*, 121301; b) M. Juppo, A. Rahtu, M. Ritala, M. Leskelä, *Langmuir* **2000**, *16*, 4034.

[18] H. Nöth, E. Wiberg, in *Anorganische Chemie. Fortschritte der Chemischen Forschung*, Springer, Berlin Heidelberg **1967**, Vol. *8/3*, p. 321.

[19] F. J. Himpsel, F. R. McFeely, A. Taleb-Ibrahimi, J. A. Yarmoff, G. Hollinger, *Phys. Rev. B* **1988**, *38*, 6084.

[20] J. M. Hill, D. G. Royce, C. S. Fadley, L. F. Wagner, F. J. Grunthaner, *Chem. Phys. Lett.* **1976**, *44*, 225.

[21] J. W. DuMont, A. E. Marquardt, A. M. Cano, S. M. George, *ACS Appl. Mater. Interfaces* **2017**, *9*, 10296.

[22] A. N. Buckley, A. J. Hartmann, R. N. Lamb, A. P. J. Stampfl, J. W. Freeland, I. Coulthard, *Surf. Interface Anal.* **2003**, *35*, 922.

[23] a) J. D. Bartl, C. Thomas, A. Henning, M. F. Ober, G. Savasci, B. Yazdanshenas, P. S. Deimel, E. Magnano, F. Bondino, P. Zeller, L. Gregoratti, M. Amati, C. Paulus, F. Allegretti, A. Cattani-Scholz, J. V. Barth, C. Ochsenfeld, B. Nickel, I. D. Sharp, M. Stutzmann,

B. Rieger, *J. Am. Chem. Soc.* **2021**, *143*, 19505; b) K. S. Liu, A. Henning, M. W. Heindl, R. D. Allert, J. D. Bartl, I. D. Sharp, R. Rizzato, D. B. Bucher, *Proc. Natl. Acad. Sci.* **2022**, *119*, 2111607119.

[24] T. Hoshino, M. Hata, S. Neya, Y. Nishioka, T. Watanabe, K. Tatsumura, I. Ohdomari, *Jpn. J. Appl. Phys.* **2003**, *42*, 3560.

[25] W. B. Berry, K. A. Emery, A. B. Swartzlander, A. J. Nelson, presented at *Conference Record of the Twentieth IEEE Photovoltaic Specialists Conference*, September 26–30, **1988**.

[26] R. Hauert, J. Patscheider, M. Tobler, R. Zehringer, *Surf. Sci.* **1993**, *292*, 121.

[27] H. Fukumizu, M. Sekine, M. Hori, P. C. McIntyre, *Jpn. J. Appl. Phys.* **2020**, *59*, 016504.

[28] K. H. Min, S. Choi, M. S. Jeong, M. G. Kang, S. Park, H. Song, J. I. Lee, D. Kim, *Curr. Appl. Phys.* **2019**, *19*, 155.

[29] a) G. F. Dionne, *J. Appl. Phys.* **1975**, *46*, 3347; b) J. Guo, D. Wang, Y. Xu, X. Zhu, K. Wen, G. Miao, W. Cao, J. Si, M. Lu, H. Guo, *AIP Adv.* **2019**, *9*, 095303.

[30] D. König, D. Hiller, S. Gutsch, M. Zacharias, S. Smith, *Sci. Rep.* **2017**, *7*, 8.

[31] R. Kimura, K. Takahashi, *Jpn. J. Appl. Phys.* **2000**, *39*, 1039.

[32] P. Zeller, M. Amati, H. Sezen, M. Scardamaglia, C. Struzzi, C. Bittencourt, G. Lantz, M. Hajlaoui, E. Papalazarou, M. Marino, M. Fanetti, S. Ambrosini, S. Rubini, L. Gregoratti, *Phys. Status Solidi A* **2018**, *215*, 1800308.